Construction of solid solution sulfide embedded in MXene@N-doped carbon dual protection matrix for advanced aluminum ion batteries

Jiening Zheng, Shunlong Ju, Long Yao, Guanglin Xia, Xuebin Yu [*]

Department of Materials Science, Fudan University, Shanghai, 200433, China

HIGHLIGHTS

- MXene and N-doped carbon confined $Ni_{0.6}Co_{0.4}S$ ($Ni_{0.6}Co_{0.4}S@MXene@NC$) was prepared.
- The incorporation of Ni into CoS improves the Al^{3+} diffusion kinetics in AIBs.
- MXene can prevent the dissolution of $Ni_{0.6}Co_{0.4}S$ towards the electrolyte.
- $Ni_{0.6}Co_{0.4}S@MXene@NC$ exhibits enhanced aluminum storage performance.

GRAPHICAL ABSTRACT
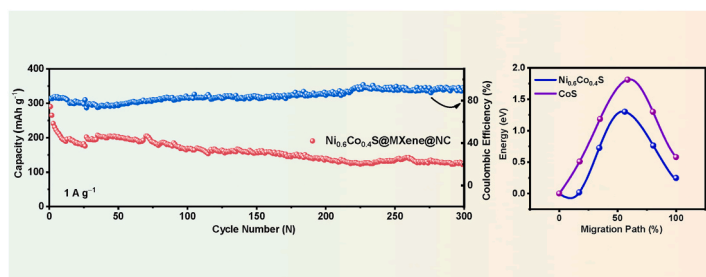
ARTICLE INFO

ABSTRACT

Engineering intriguing cathode electrode with desirable kinetics behaviors is imperative for boosting aluminum storage systems. Here, a MXene and N-doped carbon dually protected $Ni_{0.6}Co_{0.4}S$ solid solution ($Ni_{0.6}Co_{0.4}S@MXene@NC$) composite is reported as the cathode material for AIBs. The dissolution of Ni into CoS lattice leads to the electronic rearrangement, tuning its binding interaction with the Al^{3+} and modifying the Al^{3+} diffusion barrier. Consequently, the $Ni_{0.6}Co_{0.4}S$ renders the high overall Al^{3+} adsorbability, and contributes to fast Al^{3+} diffusion kinetics. Additionally, the robust MXene@NC protective shell not only provides faster electron transfer pathway, but also contributes to high chemical and structural stability, attributed to the inhibition of active species dissolution and favorable tolerance to volume change. This novel design enables the $Ni_{0.6}Co_{0.4}S@MXene@NC$ composite a high initial discharge capacity of 481.2 mA h g^{-1} at 400 mA g^{-1}. Even at 1000 mA g^{-1}, the capacity still maintains at 125.2 mA h g^{-1} after 300 cycles. Meanwhile, the investigation of reaction mechanism reveals that the cell involves the intercalation of Al^{3+} into $Ni_{0.6}Co_{0.4}S$ to generate $Al_lNi_mCo_nS$ and elemental Ni and Co. This work propels the process of enhancement of electrochemical performance for AIBs via smart designing and constructing cathode materials.

1. Introduction

Lithium-ion batteries (LIBs) have dominated in electrical energy storage devices since the 1990s due to their high specific energy and power density [1,2]. However, the limited lithium resources and safety problems caused by lithium dendrite and flammable organic electrolytes restrict their further application for large-scale energy storage systems. As a result, new rechargeable batteries, e.g. sodium-ion batteries,

---

potassium-ion batteries, magnesium-ion batteries, and aluminum-ion batteries (AIBs), are being considered as promising alternative candidates due to their high abundance and low cost [3–5]. Among them, AIBs with aluminum metallic anode and room temperature ionic liquid electrolyte have gradually gained much attention because of aluminum being the most abundant metal in the earth's crust [3]. In addition, the redox of Al is usually based on three electrons transfer during the electrochemical reaction, which provides higher specific capacity [6]. However, the development of AIBs is curbed by the lack of suitable cathode materials. Although carbon materials have been demonstrated to be effective AIBs cathode materials for the intercalation/deintercalation of $AlCl_4^-$ and display good cycling stability and superior rate capability, they often suffer from low capacity (<100 mAh g^{-1}) as their monovalent $AlCl_4^-$ storage properties [7–9]. Moreover, the intercalation of large size of $AlCl_4^-$ may cause severe structural damage of carbons.

Alternatively, transitional metal chalcogenides (TMCs), due to their abundant source, easy preparation, and high theoretical capacity originating from the intercalation/deintercalation of Al^{3+} rather than $AlCl_4^-$, have been regarded as another kind of promising cathode materials for AIBs [10]. Despite these promising aspects, trivalent Al^{3+} typically displays strong electrostatic interactions with the host lattice of TMCs, leading to structural destruction and slow Al^{3+} diffusion [10,11]. In general, several strategies have been developed for the improvement of Al^{3+} diffusion kinetics and structural stability for TMCs cathodes. For example, preparing nanoarchitecture to shorten the diffusion distance for Al^{3+} ions such as nanorods [12,13], nanobelts [14,15], and nanosheets [16]; and mixing with conductive carbonaceous material to buffer the volume change, etc. Although these strategies can enhance the transfer characteristics of Al^{3+} ions and mitigate the structural deformation, it is not available for the improvement of the intrinsic ionic conductivity of cathode materials for AIBs, resulting in unsatisfactory electrochemical performance.

It is well known that the structures of cathode materials determine their interactions with metal ions, which in turn intimately influence the electrochemical behaviors of cathode in terms of capacity, rate capability, and cycling stability [17]. Alloying or doping of TMCs is able to realize accurate band gap tuning over a longer energy range, which provides the possibility for improving ions diffusion kinetics [18,19]. Density functional theory (DFT) calculations have shown that W, a group-VI transition metal, can incorporate into MoS_2 and tune its electronic structure, displaying lower Li^+ diffusion barrier compared with that of MoS_2 [18]. Experimentally, a series of doped or alloyed TMCs, including but not limited to $Ni_{0.75}Fe_{0.25}Se_2$ microflowers [20], CoFeS@rGO [21], Mn-doped MoS_2 nanosheets [19], and $VMoS_2$ [22] have been synthesized and applied into various alkali metal ion batteries for their fast ions diffusion performance. These results suggest that elaborate structural modification via alloying or doping to render favorable interaction between Al^{3+} and the host lattices is a potential strategy to improve the properties of TMCs cathodes, whereas the successful implementation has never been reported in AIBs.

Co and Ni have similar atomic radius (126 vs 124 p.m.) and their sulfides own the same crystal structures, which is favorable of forming a complete solid solution. The solid solution state with atomic interaction may provide new opportunities to finely modify the crystal and electronic structure of the cathode for fast Al^{3+} diffusion. With these in mind, we have successfully fabricated $Ni_{0.6}Co_{0.4}S$ solid solution as a desirable model for atomic structure engineering toward improved AIBs. Density functional theory (DFT) calculations were performed to evaluate the Al^{3+} intercalation and diffusion process in $Ni_{0.6}Co_{0.4}S$ solid solution. Consequently, the $Ni_{0.6}Co_{0.4}S$ solid solution improves overall Al^{3+} storage capability and decreases the Al^{3+} diffusion barrier, leading to fast Al^{3+} intercalation/deintercalation kinetics.

Additionally, the active species dissolution during cycling process also is the serious problem in AIBs, which leads to rapid capacity fading [23]. MXenes, a new family of 2D layer materials, have been discovered

by Gogotsi et al. in 2011 [24]. The formula of MXenes is $M_{n+1}X_nT_x$, where M is an early transition metal, X is C and/or N, n = 1, 2 or 3, and T_x represents the surface functional groups (OH, O and F) [25]. MXenes have been widely investigated as electrode materials due to their superior characteristics, i.e., high specific surface area, metallic conductivity, and hydrophilic surface [26–28]. Nazar's group firstly reported that MXenes phases boost the electrochemical performance of lithium-sulfur batteries by virtue of forming metal–sulfur bonds via a Lewis acid–base interaction between the highly active metal atoms on the surfaces of MXenes and sulfur species [29,30]. Thus, due to the abundant surface functional groups and high specific surface area, MXenes could be a good choice for preventing transitional metal chalcogenides dissolution and shuttling in the ion liquid electrolyte which have rarely been applied in the AIBs.

Therefore, a strategy of in situ anchoring and coating was proposed, in which an integrated MXene and N-doped carbon shell were simultaneously composited with $Ni_{0.6}Co_{0.4}S$ ($Ni_{0.6}Co_{0.4}S@MXene@NC$). In the designed hybrid, $Ni_{0.6}Co_{0.4}S$ can reversibly store aluminum ions with improved Al^{3+} intercalation/deintercalation kinetics, while MXene and NC can not only facilitate electron transfer, but also contribute to high chemical and structural stability due to inhibiting active species dissolution and favorable tolerance to volume change, respectively. As a result, the designed AIBs cathode delivers a high initial capacity of 481.2 mA h g^{-1} at 400 mA g^{-1} and a stable cycling capacity of 125.2 mA h g^{-1} at 1000 mA g^{-1} after 300 cycles.

2. Experimental

2.1. Synthesis of delaminated $Ti_3C_2T_x$ MXene

Typically, 1 g Ti_3AlC_2 MAX power was added slowly into 20 mL 9 M hydrochloric acid solution containing 1 g LiF, stirring for 24 h at 35 °C. After that, the residues were collected by centrifugation and washed with deionized (DI) water several times until PH > 6, then the precipitates were ultrasonicated in an ice-bath for 2 h under the protection of N_2. Finally, the supernatant ($\approx$4 mg mL^{-1}) was collected by centrifugation at 3500 rpm for 1h.

2.2. Synthesis of NiCo Prussian blue analogues (NiCo PBA)@MXene and NiCo PBA@MXene@PDA

Typically, 0.1 g polyvinyl pyrrolidone (PVP) was dissolved in 100 mL MXene (2 mg mL^{-1}). Then 3 mmol of $Ni(NO_3)_2 \cdot 6H_2O$ was added to the mixture, followed by stirring for 1 h to obtain the Ni^{2+} adsorbed MXene products. After that, 2 mmol of $K_3[Co(CN)_6]_2$ and 4.5 mmol of sodium citrate were added to the above mixture under continuous stirring for 10 min. Subsequently, the mixed solution was aged for 24 h at room temperature (RT). Finally, the foam-like products were obtained by centrifugation, washed several times with deionized water and ethanol, and then treated with freeze-drying for 48 h. For the preparation of NiCo PBA@MXene@PDA, 80 mg of NiCo PBA@MXene was dissolved in 100 ml of tri-butter solution (10 mM, pH 8.5) aided by ultrasonic treatment for 30 min, followed by adding 80 mg of dopamine hydrochloride and stirred continuously for 24 h at RT. The black products were achieved by centrifugation and washed several times with deionized water and ethanol. And the final foam-like products were obtained via further freeze-drying for 48 h.

2.3. Synthesis of $Ni_{0.6}Co_{0.4}S@MXene@NC$

The as-prepared NiCo PBA@MXene@PDA and sulfur with mass ratio of 1:5 were put separately into the tubular furnace under an Ar flow. The furnace was heated to 350 °C with a ramp rate of 2 °C min^{-1} and kept for 2 h to get the sulfide composites. Then, the obtained products were annealed at 600 °C for 2 h with a ramp rate of 2 °C min^{-1} under Ar flow to form $Ni_{0.6}Co_{0.4}S@MXene@NC$. For comparison, the

CoS@MXene@NC, $Ni_{0.6}Co_{0.4}S@NC$, $Ni_{0.6}Co_{0.4}S@MXene$, and MXene@NC were fabricated in the similar way except using $Co_3[Co(CN)_6]_2·9H_2O@MXene$ (CoCo PBA@MXene), NiCo PBA, NiCo PBA@MXene, and MXene as precursors, respectively.

2.4. Materials characterizations

The morphology, composition, structure, and element chemical states were investigated by field emission scanning electron microscopy (FE-SEM; JEOL 7500FA, Tokyo, Japan), transmission electron microscopy (TEM; JEOL 2011 F, Tokyo, Japan) coupled with an EDX spectrometer, powder X-ray diffraction (XRD; D8 Advance, Bruker AXS) with Cu Kα radiation, and X-ray photoelectron spectroscopy (XPS; PerkinElmer PHI 5000C ESCA). Fourier transform infrared spectroscopy (FT–IR) tests were performed on Nicolet 6700 spectrometer. The chemical composition of the samples was obtained by inductively coupled plasma-optical emission spectroscopy measurements (ICP-OES, Thermo scientific-ICAP 7000).

2.5. Electrochemical measurements

Electrochemical measurements were carried on customized Swagelok-type cells assembled with the active sample as working electrode, aluminum metal foil (99.99%) as counter electrode, paper glass fiber (GF/D) as separator, and the ion liquid electrolyte (the mixture of 1-ethyl-3-methylimidazolium chloride ([EMIm]Cl) and anhydrous $AlCl_3$ with the molar ratio of 1:1.3) in an argon-filled glove box (<0.1 ppm of H_2O and O_2). The working electrode was prepared by coating the slurry containing of the active sample, super P acetylene black, and polyvinylidene fluoride (PVDF) with the mass ratio of 8:1:1 dissolved in N-methylpyrrolidone (NMP) solution on molybdenum foil, following by drying at 80 °C under vacuum overnight. Galvanostatic charge/discharge tests ran on a battery testing system (Land-CT2001A) over the voltage window of 0.01–2.1 V at room temperature. Cyclic voltammetry (CV) measurements were tested at a scan rate of 0.5 mV s^{-1} within the same voltage window. Electrochemical impedance spectroscopy (EIS) tests were performed in the frequency window of 100 kHz–100 mHz. The CV and EIS tests were achieved on a CHI 660D electrochemical workstation.

2.6. Computational method

Density functional theory (DFT) calculations were carried out using projector-augmented wave (PAW) method as implemented in Vienna ab initio simulation package (VASP) [31,32]. A generalized gradient approximation (GGA) of Perdew-Burke-Ernzerhof (PBE) functional was employed to describe the exchange-correlation interaction [33]. An energy cutoff of 500 eV and $3 \times 3 \times 3$ k-points mesh were applied to all calculations. The structures were relaxed until the forces and total energy on all atoms were converged to less than 0.05 eV Å^{-1} and 1×10^{-5} eV. DFT + U approximation was used to describe the d orbitals of transition metal species [34]. Following the previous works, U (Co) = 5.7 eV and U (Ni) = 6.1 eV was applied, and the spin polarization and magnetism of Ni and Co atoms were considered in all calculations [35–38]. Diffusion barriers for Al^{3+} hopping in CoS and $Ni_{0.6}Co_{0.4}S$ lattice are calculated using the climbing-image nudged elastic band (CI-NEB) method, and 4 images were used in all kinetics calculations [39].

To evaluate the intercalation process of Al^{3+} in CoS and $Ni_{0.6}Co_{0.4}S$, the formation energy (E_f) was calculated. According to the reaction equations, when a Al atoms intercalate into sulfide crystal to displace b Ni atoms and c Co atoms, E_f was defined as the energy difference as follows, $E_f = E(Al + sulfide) + a*E(Ni) + b*E(Co) – cE(Al) – E(sulfide)$ where *E(Al + sulfide)* is the total energy of CoS or $Ni_{0.6}Co_{0.4}S$ with Al^{3+} intercalated. *E(sulfide)* is the energy of pristine CoS or $Ni_{0.6}Co_{0.4}S$. *E(Ni), E(Co)* and *E(Al)* is the energy per atom for the bulk Ni, Co and Al,

respectively. Therefore, a lower value of E_f indicates that the intercalation process is easier.

3. Results and discussion

The fabricating procedure of $Ni_{0.6}Co_{0.4}S@MXene@NC$ is schematically shown in Fig. 1. Firstly, $Ti_3C_2T_x$ MXene nanosheets were obtained via a selected LiF/HCl etching of the MAX phase Ti_3AlC_2 followed by ultrasonic stripping, which display a loosely and flexible layered structure, as shown in the scanning electron microscope (SEM) image (Fig. 2a). The successful phase change during the fabrication process was determined by the X-ray diffraction (XRD). For delaminated MXene, only one strong peak (002) located at around $2\theta = 6.3°$ can be observed without the presence of characteristic peaks of MAX phase (Fig. S1a) [40]. Then, $Ni(NO_3)_2$ was mixed with MXene which owned increased surface functional groups modified by polyvinyl pyrrolidone (PVP) to obtain electronegative MXene sheets to adsorb Ni^{2+} composites via electrostatic interaction. Then, the NiCo PBA nanocubes were nucleated and grown in situ on MXene nanosheets after adding $K_3[Co(CN)_6]$ and sodium citrate. The obtained NiCo PBA@MXene sample shows a homogenous distribution of NiCo PBA nanocubes on the wrinkled MXene surface (Fig. 2b) treated with the freeze-drying process. Next, a layer of polydopamine (PDA) was coated on the surface of NiCo PBA@MXene to form NiCo PBA@MXene@PDA. After freeze-drying, the NiCo PBA@MXene@PDA has the similar morphology with NiCo PBA@MXene except the rough surface caused by PDA coating (Fig. 2c). The two products display the similar characteristic diffraction peaks indexed to $Ni_3[Co(CN)_6]_2$ (Fig. S1b), indicating that the PDA coating has no influence on the inner NiCo PBA crystal structure. Due to the low proportion, the diffraction peak of MXene is difficult to be observed. After subsequent sulfurization and carbonization, the obtained $Ni_{0.6}Co_{0.4}S@MXene@NC$ composite maintained the original morphology (Fig. 2d–f). Further examined by the transmission electron microscopy (TEM, Fig. 2g and h), the MXene (marked with yellow arrows) supported $Ni_{0.6}Co_{0.4}S$ hybrids are uniformly coated by a carbon layer with the thickness of about 15 nm (marked with red arrows). The high resolution TEM (HRTEM) image (Fig. 2i) reveals clear fringes with interplanar spacing of 0.257 nm, corresponding to the (101) plane of $Ni_{0.6}Co_{0.4}S$. The element mapping images further reveal the homogenous distribution of Ni, Co, S, C, Ti, and N elements in the composite (Fig. 2j).

For comparison, the CoS@MXene@NC, $Ni_{0.6}Co_{0.4}S@MXene$, and $Ni_{0.6}Co_{0.4}S@NC$ were synthesized in the similar way except using $Co_3[Co(CN)_6]_2@MXene@PDA$, $Ni_3[Co(CN)_6]_2@MXene$, and $Ni_3[Co(CN)_6]_2@PDA$ as precursors, respectively. The morphology and structure information of these precursors were given in Fig. S2. As displayed in SEM (Figs. S3a and c) and TEM images (Figs. S3b and d), the CoS@MXene@NC shows the similar morphology with $Ni_{0.6}Co_{0.4}S@MXene@NC$ except for the larger particle size of CoS based nanocubes, while the $Ni_{0.6}Co_{0.4}S@NC$ presents the aggregated carbon coated multi-core cubic morphology, which confirms that MXene nanosheets can prevent $Ni_{0.6}Co_{0.4}S@NC$ nanoparticles from aggregation. Additionally, $Ni_{0.6}Co_{0.4}S@MXene$ shows irregular and non-cubic particles distributing on the partially oxidized MXene nanosheets (Figs. S3e and f), indicating that the PDA derived carbon can not only keep $Ni_{0.6}Co_{0.4}S$ nanocubes from collapse during the high temperature treatment [41], but also effectively resist high temperature oxidation of MXene [42]. The XRD patterns in Fig. 3a show that the CoS@MXene@NC presents dominant diffraction peaks with 2θ at 30.5°, 35.2°, 47.0°, and 54.3°, which correspond well to the (100), (101), (102), and (110) planes of CoS (PDF card no.75-0605). For the $Ni_{0.6}Co_{0.4}S@MXene@NC$ and $Ni_{0.6}Co_{0.4}S@NC$, the XRD patterns match well with that of CoS phase except for a slight left shift, confirming the formation of solid solution through the homogenous doping of Ni atoms into the CoS lattice. Additionally, because of the low content, the diffraction peaks of MXene can not been observed clearly. As displayed in Table S1, the average Ni/Co atomic ratio is determined to be 1.44:1,
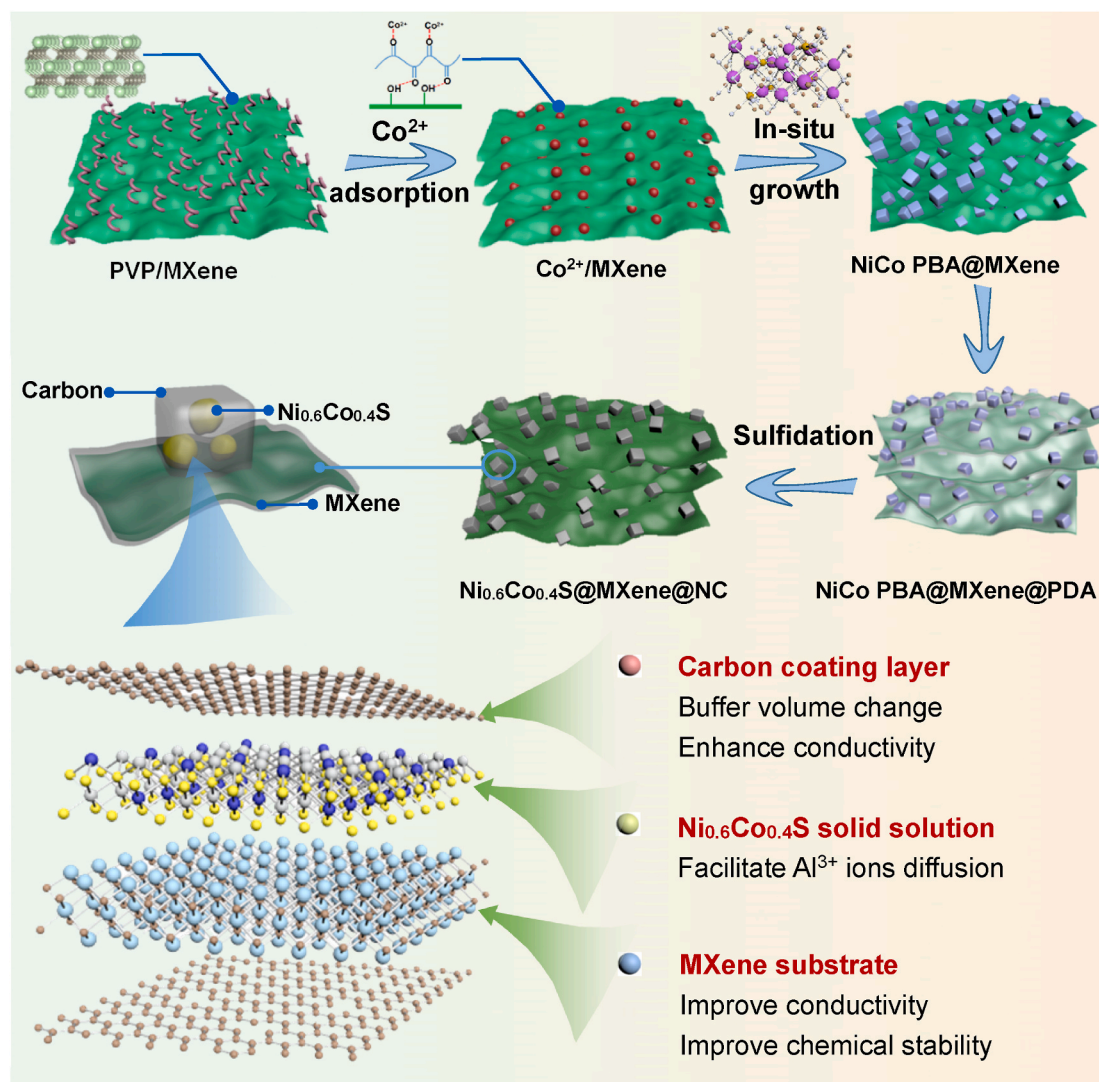
Fig. 1. Schematic illustration for the synthesis of $Ni_{0.6}Co_{0.4}S@MXene@NC$ composite.

close to the stoichiometric ratio of precursors (1.5:1).

As shown in Fig. 3b, the high-resolution XPS (HR-XPS) spectrum of Ti 2p can be fitted into four peaks centered at 458.3, 463.5, 458.6, and 464.5 eV, corresponding to Ti^{3+} (Ti $2p_{3/2}$), Ti^{3+} (Ti $2p_{1/2}$), Ti-O (Ti $2p_{3/2}$), and Ti-O (Ti $2p_{1/2}$) bonds, respectively [43]. Compared with the Ti 2p spectrum of MXene, the shift to higher binding energy indicates that Ti undergoes charge transfer after the load of $Ni_{0.6}Co_{0.4}S$ [44]. The O 1s HR-XPS spectrum of MXene discloses the presence of $Ti-C-O_x$ and $Ti-C-(OH)_x$ bonds at 530.1 and 531.7 eV, respectively (Fig. 3c) [45]. For Ni 2p, the two distinct and sharp peaks at 854.0 and 871.5 eV are assignable to $2p_{3/2}$ and $2p_{1/2}$ of Ni^{2+} species (Fig. 3d) [15]. In addition, two satellite peaks appear at 860.2 and 878.2 eV, which are similar with those of reported results [46]. In the Co 2p spectrum (Fig. 3e), two main peaks located at 780.8 and 796.7 eV can be indexed to Co-S (Co $2p_{3/2}$), Co-S (Co $2p_{1/2}$) characteristic peaks of $Ni_{0.6}Co_{0.4}S@MXene@NC$, respectively [47]. The peaks at 779.0 and 785.8 eV can be ascribed to the Co-O bond, resulted from the slight surface oxidation of Co [47,48]. Meanwhile, two peaks observed at 783.0 and 802.2 eV can be indexed to the satellite peaks of Co 2p [48]. The S 2p XPS HR-XPS spectrum (Fig. 3f) shows three kinds of sulfur species. The doublet at lower binding energy of 161.8 ($2p_{3/2}$) and 164.6 eV ($2p_{1/2}$) is pointed to the terminal S^{2-} ligands, and the doublet at higher binding energy of 163.8 ($2p_{3/2}$) and 165.1 eV ($2p_{1/2}$) is pointed to bridging S^{2-} ligands and/or apical S^{2-} ligands, respectively [49,50]. The sulfate group (168.6 eV) is attributed

to the slight surface oxidation of S^{2-} because of the direct exposure in air [51]. For the HR-XPS C 1s spectrum, the peaks at 284.6, 285.3, and 286.3 eV are indexed to the C-C, C-N, and -C=O chemical bonds, respectively (Fig. 3g) [52]. The existing of the C-N bond demonstrates the successful preparation of N-doped carbon matrix derived from the carbonization of the PDA coating layer, also verified by the N 1s HR-XPS spectrum (Fig. 3h). The N 1s spectrum demonstrates three peaks at 398.6, 400.1, and 401.0 eV, which correspond to the Ti-N, pyridinic-N, and pyrrolic-N, respectively [53]. The existence of Ti-N bond further confirms the successful coating of PDA derived N-doped carbon layer on the MXene surface. Additionally, XPS survey spectrum of $Ni_{0.6}Co_{0.4}S@MXene@NC$ is displayed in Fig. S4.

It is worth to mention that the PVP plays the critical role in the fabricating of homogeneous NiCo PBA nanocubes growth on ultrathin MXene nanosheets. As shown in Fig. S5a, the obtained NiCo PBA@MXene solution is uniform in the present of PVP (I). In sharp contrast, the absence of PVP results in the separation MXene (black) and NiCo PBA (blue) in the mixture (II). The morphology of NiCo PBA@MXene, NiCo PBA@MXene@PDA, and Ni-CoS@MXene@NC obtained without PVP were further checked by the SEM (Figs. S5b–d). Clearly, all of these products display uneven growth of NiCo based nanoparticles on the MXene and the MXene nanosheets undergo serious restack. These results clearly demonstrate the crucial role of PVP in the formation of uniform NiCo PBA on ultrathin MXene nanosheets. It can be speculated that the
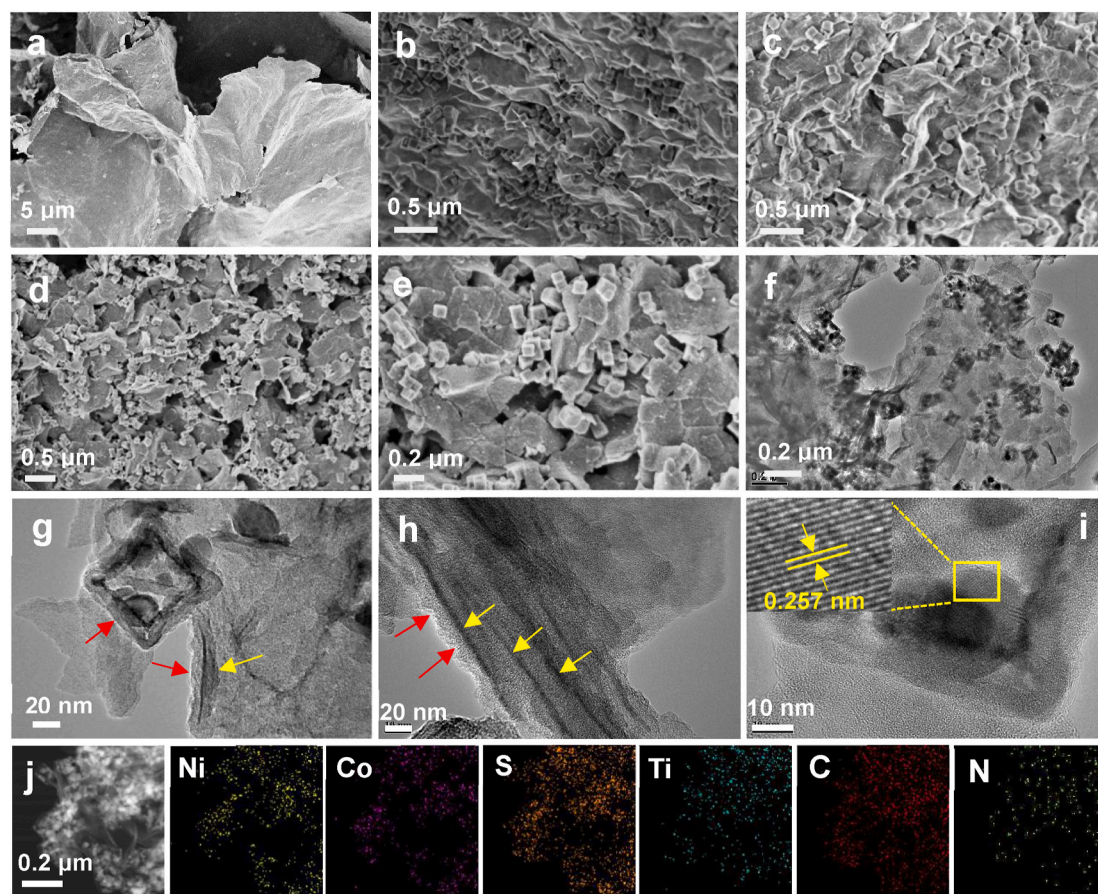
Fig. 2. (a–c) SEM images of MXene, NiCo PBA@MXene, and NiCo PBA@MXene@PDA, respectively. (d,e) SEM images of $Ni_{0.6}Co_{0.4}S$@MXene@NC. (f,g) TEM images, (h,i) HRTEM images for $Ni_{0.6}Co_{0.4}S$@MXene@NC. (j) STEM-EDX elemental mapping images of $Ni_{0.6}Co_{0.4}S$@MXene@NC.

PVP with the amide carbonyl groups enriches the surface functional groups of MXene, resulting in firm and homogeneous NiCo PBA growth on MXene. Also, the restacking of MXene can be avoided via NiCo PBA homogeneous loading. In addition, the existence of PVP in NiCo PBA@MXene composite after wash by centrifugation was further verified by the Fourier transform infrared spectroscopy (FT–IR) as shown in Fig. 3i. Specifically, the C=O (1650 cm^{-1}) and C−N (1270 cm^{-1}) groups originating from PVP in MXene (PVP) and NiCo PBA@MXene (PVP) composites enhance/arise significantly compared with those of bare MXene. Therefore, we can conclude that NiCo PBA@MXene is fabricated by the hydrogen bonds between MXene and PVP and the coordinate bonds between PVP and NiCo PBA.

The electrochemical performance of $Ni_{0.6}Co_{0.4}S$@MXene@NC, CoS@MXene@NC, $Ni_{0.6}Co_{0.4}S$@NC, and $Ni_{0.6}Co_{0.4}S$@MXene composites were evaluated in the Swagelok-type cell using the active material as the cathode, Al foil as the anode and ionic liquid [EMIm]Cl as the electrolyte. The CV curves of $Ni_{0.6}Co_{0.4}S$@MXene@NC, CoS@MXene@NC, and $Ni_{0.6}Co_{0.4}S$@NC in the operation voltage window of 0.01–2.1 V are presented in Fig. 4a. All of these electrodes show a main oxidation peak at 0.7–1.0 V and a reduction peak at around 0.3–0.5 V. The first three galvanostatic discharge and charge curves of $Ni_{0.6}Co_{0.4}S$@MXene@NC at 400 mA g^{-1} are displayed in Fig. 4b. The observed discharge/charge plateaus match well with the peaks in the CV curve. From the first to the third cycle, it delivers high specific discharge capacities of 481.2, 430.0, and 406.1 mA h g^{-1}, respectively, reflecting the effective utilization of active materials. The irreversible capacity loss for the subsequent cycles can be due to the formation of solid electrolyte interface (SEI) layer and the decomposition of electrolyte or possible side reactions [13,54]. In addition, the first three galvanostatic curves of $Ni_{0.6}Co_{0.4}S$@MXene@NC at 1000 mA g^{-1} are presented in Fig. 4c.

Moreover, the CoS@MXene@NC displays the similar discharge/charge behavior (Fig. S6), indicating that the CoS@MXene@NC undergoes almost the same electrochemical process compared with that of $Ni_{0.6}Co_{0.4}S$@MXene@NC.

Fig. 4d exhibits the cycling performance of these materials at a current of 1000 mA g^{-1}. For $Ni_{0.6}Co_{0.4}S$@MXene@NC, the discharge capacity decreases gradually in the initial 10 cycles, and maintains 194.8 mA h g^{-1} in the 10th cycle. Prolonging the cycling process up to 300 cycles, it still provides a reversible discharge capacity of 125.2 mA h g^{-1} with the CE around 90%, demonstrating superior long-term cycling stability. According to the aluminum storage mechanism mentioned below, the reversible aluminum storage of the initial cycle is about 0.342 per $Ni_{0.6}Co_{0.4}S$, which decreases to 0.147 per $Ni_{0.6}Co_{0.4}S$ after 300 cycles, suggesting that some of the Al^{3+} ions are trapped in the cathode. Thus, the capacity decreases gradually with the increasing cycles. In addition, the formation of the irreversible SEI layer, the decomposition of electrolyte, and the active material dissolution also lead to the cycling performance decay [55,56]. The Al^{3+} storage performance of MXene and MXene@NC have been measured by long term cycling stability test (Figs. S7a and b). Note that both of them contribute negligible capacity, indicating that a limited quantity of Al^{3+} ions can intercalate into MXene and NC and most of them are stored in $Ni_{0.6}Co_{0.4}S$. Moreover, for the CoS@MXene@NC, the discharge capacity of initial cycle is 280.9 mA h g^{-1} and then tends to rapid decline, finally remaining only 104.2 mA h g^{-1} at the 300th cycle. The higher specific capacity and better cycling stability of $Ni_{0.6}Co_{0.4}S$@MXene@NC is mainly ascribed to the Ni incorporation, which greatly improves the electrochemical active sites and redox kinetics [44]. Besides, as the absence of MXene or N-doped carbon layer coating, the $Ni_{0.6}Co_{0.4}S$@NC and $Ni_{0.6}Co_{0.4}S$@MXene exhibit inferior cycling performance. The fast
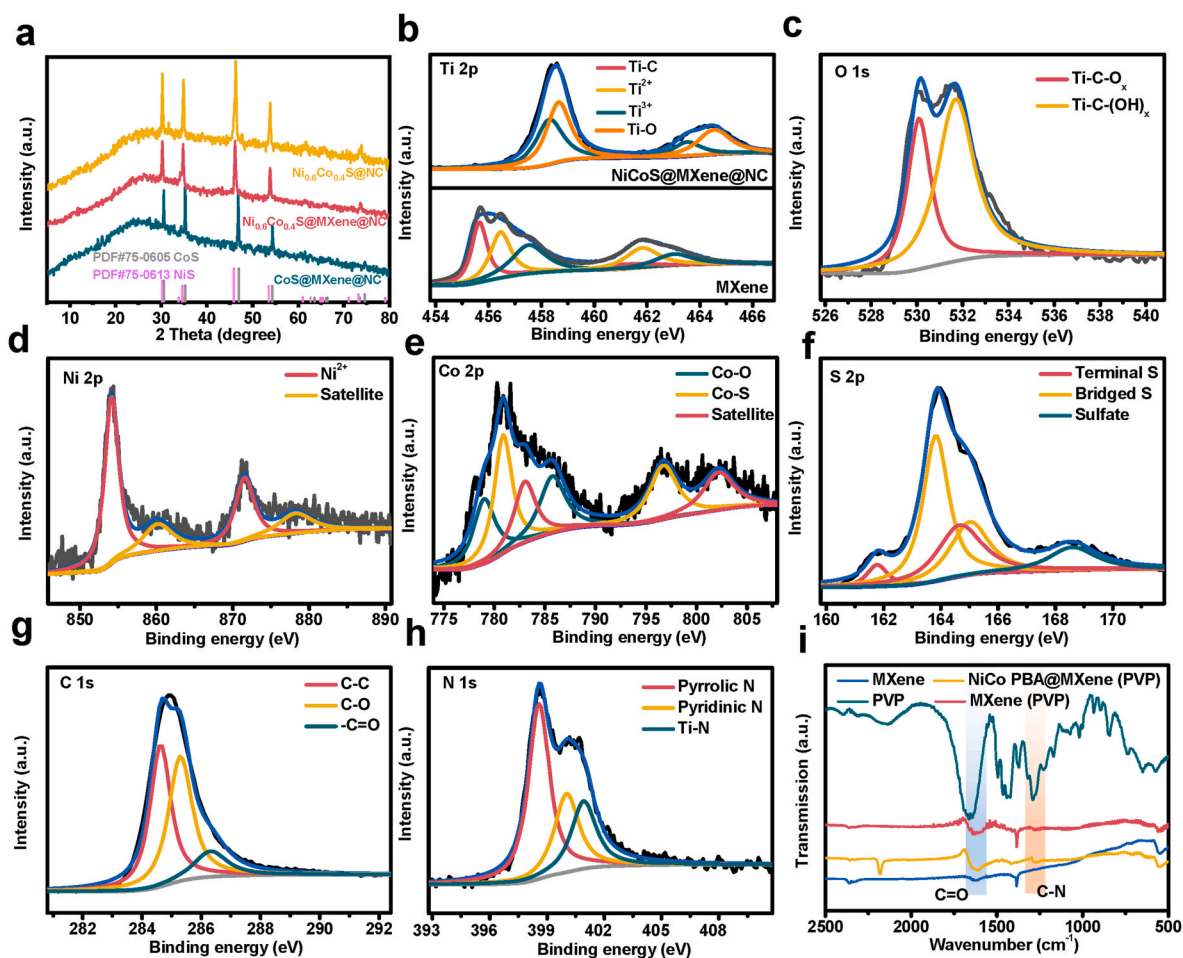
Fig. 3. (a) XRD patterns of $Ni_{0.6}Co_{0.4}S$@MXene@NC, CoS@MXene@NC, and $Ni_{0.6}Co_{0.4}S$@NC. (b–h) High-resolution XPS spectra of (b) Ti 2p, (c) O 1s, (d) Ni 2p, (e) Co 2p, (f) S 2p, (g) C 1s, and (h) N 1s for $Ni_{0.6}Co_{0.4}S$@MXene@NC. (i) FT–IR spectra of MXene, PVP decorated MXene, NiCo PBA@MXene (PVP decorated MXene), and PVP.

capacity drop of these cathodes indicates structural instability and active materials dissolution upon cycling which will be discussed in the following paragraph.

Furthermore, to understand the excellent cycling performance at high current density of $Ni_{0.6}Co_{0.4}S$@MXene@NC compared to those of CoS@MXene@NC, $Ni_{0.6}Co_{0.4}S$@NC, and $Ni_{0.6}Co_{0.4}S$@MXene composites, electrochemical impedance spectroscopy (EIS) analysis of pristine and cycled cathodes (100 cycles) have been studied. As shown in Fig. 4e, both of the Nyquist plots mainly consist of a semicircle in high-frequency region and a straight line in low-frequency region. The equivalent circuit obtained from Nyquist plots fitting is given in Fig. S8. Here, R_s represents the ohmic resistance of the electrolyte and cell components, R_{SEI} corresponds the resistance of SEI film, R_{ct} is the charge-transfer resistance, C_{SEI} and C_{ct} are the constant phase-angle elements, and W is the Warburg element. As displayed in the enlarged EIS results in insets of Fig. 4e,g, R_{ct} value for these electrodes before cycling and after 100 cycles are all less than 5 Ω, displaying low charge transfer resistance of those cathodes. However, compared with the CoS@MXene@NC, $Ni_{0.6}Co_{0.4}S$@NC, and $Ni_{0.6}Co_{0.4}S$@MXene electrodes, the $Ni_{0.6}Co_{0.4}S$@MXene@NC electrode shows the lowest R_{ct} value in the cycling process, reflecting excellent electronic conductivity and reaction kinetics [57]. Moreover, the straight line in low-frequency region reflects the solid-state Al^{3+} diffusion rate within the bulk cathode of composite, and the more inclined slope indicates faster ion diffusion kinetics [58]. To obtain the more intuitive results, the slope line can be further converted the relationship between Z′ and $\omega^{-1/2}$. Clearly, among the whole cycling, the Al^{3+} diffusion rates increase in the following order: $Ni_{0.6}Co_{0.4}S$@MXene <

CoS@MXene@NC < $Ni_{0.6}Co_{0.4}S$@NC < $Ni_{0.6}Co_{0.4}S$@MXene@NC (Fig. 4f,h). Therefore, it can be inferred that the Ni incorporation plays a pivotal role in the facilitating of trivalent Al^{3+} diffusion, which has been further confirmed by the density functional theory (DFT) calculation result.

Ex-situ XPS, XRD, and STEM-EDX techniques were applied to further probe the possible Al^{3+} storage mechanism in $Ni_{0.6}Co_{0.4}S$@MXene@NC cathode. Fig. 5a and b shows the Ni 2p and Co 2p XPS spectra of the pristine, initial fully charged, and discharged $Ni_{0.6}Co_{0.4}S$@NC, respectively. After discharging process, new peaks corresponding to metallic Ni (Ni^0 $2p_{3/2}$ at 853.4 eV) and Co (Co^0 $2p_{3/2}$ at 777.5 eV and Co^0 $2p_{1/2}$ at 790.2 eV) are observed, which indicate the reduction of Ni^{2+} to Ni^0 and Co^{2+} to Co^0, respectively [23,59]. Moreover, as displayed in Fig. 5c and d, the Al 2p peak in the fully discharged state is stronger than that in the fully charged state, while the Cl 2p signal keeps almost unchanged, indicating that the intercalated species into $Ni_{0.6}Co_{0.4}S$ phase is Al^{3+} rather than $AlCl_4^-$ [23,60]. STEM-EDX was performed to further verify the intercalation of Al^{3+} ions in $Ni_{0.6}Co_{0.4}S$. It shows that Ni, Co, S, and Al signals display the similar distribution across the $Ni_{0.6}Co_{0.4}S$@NC particles in the discharged state as presented in Fig. S9a, which reflects the insertion of Al^{3+} into the $Ni_{0.6}Co_{0.4}S$. For the charged state, the mapping images display very weak Al signals, confirming that most of the Al^{3+} ions have been extracted out from $Ni_{0.6}Co_{0.4}S$ (Fig. S9a). Ex situ XRD was further conducted to monitor the crystal structure changes of the $Ni_{0.6}Co_{0.4}S$@NC cathode during the discharging and charging process. As displayed in Fig. 5e and f, the characteristic diffraction peaks of $Ni_{0.6}Co_{0.4}S$ become weaker and broader, and these peaks especially

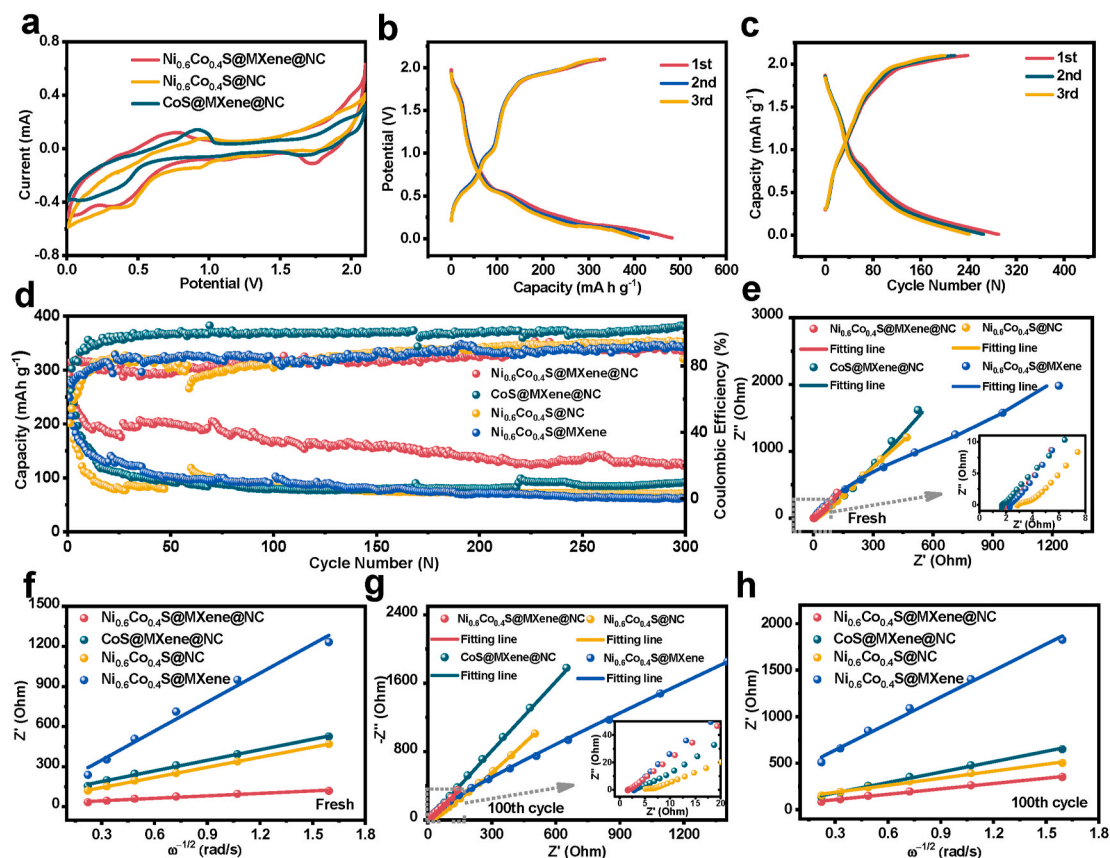**Fig. 4.** (a) CV curves of $Ni_{0.6}Co_{0.4}S@MXene@NC$, $CoS@MXene@NC$, and $Ni_{0.6}Co_{0.4}S@NC$ obtained at a scanning rate of 0.5 mV s^{-1}. The selected galvanostatic discharge–charge profiles of $Ni_{0.6}Co_{0.4}S@MXene@NC$ (b) at 0.4 A g^{-1} and (c) at 1.0 A g^{-1}. (d) Cycling performance of $Ni_{0.6}Co_{0.4}S@MXene@NC$, $CoS@MXene@NC$, $Ni_{0.6}Co_{0.4}S@NC$, and $Ni_{0.6}Co_{0.4}S@MXene$ at 1000 mA g^{-1}. Nyquist impedance plots and relationship between real impedance with low frequency of $Ni_{0.6}Co_{0.4}S@MXene@NC$, $CoS@MXene@NC$, $Ni_{0.6}Co_{0.4}S@NC$, and $Ni_{0.6}Co_{0.4}S@MXene$ (e,f) before cycling and (g,h) after 100 cycles (inset in (e,g) are the enlarged Nyquist impedance plots).

(100) and (101) peaks slightly shift to lower angles after discharging, indicating the increase of the according interplanar spacing after Al^{3+} insertion. After charging, the peaks almost move back to their original positions, revealing that most of the Al^{3+} ions can be reversibly extracted from $Ni_{0.6}Co_{0.4}S$ during the charge process. Based on the above analysis, the possible charge/discharge main reactions of the batteries can be denoted as the following equations:

$$4Al_2Cl_7^- \rightleftharpoons Al^{3+} + 7AlCl_4^- \tag{1}$$

$$Ni_{0.6}Co_{0.4}S + lAl^{3+} + 3le^- \rightleftharpoons Al_lNi_mCo_nS + (0.6 - m)Ni + (0.4 - n)Co \tag{2}$$

To further interpret how $Ni_{0.6}Co_{0.4}S$ solid solution improves the aluminum storage performance, a theoretical Al^{3+}−storage ability of the $Ni_{0.6}Co_{0.4}S$ was calculated based on density functional theory (DFT). In Fig. S10a, CoS with space group $P6_3/mmc$ was employed in the calculations as a reference. By randomly replacing some of the Co atoms in CoS with Ni atoms in proportion, the model with the lowest energy is used to represent $Ni_{0.6}Co_{0.4}S$ as illustrated in Fig. S10b. To simulate the Al^{3+} intercalated model, according to equation (2), two Al atoms were embedded into a 4 × 4 × 2 cell to replace three transition metal atoms. And the formation energy (E_f) of the intercalation process was computed. In CoS, E_f was calculated to be 1.89 eV. This result evidences that Al atom needs a certain amount of energy to intercalate in CoS. While in $Ni_{0.6}Co_{0.4}S$, Al tends to displace Ni first and the corresponding E_f is −1.48 eV. A lower E_f of $Ni_{0.6}Co_{0.4}S$ confirms that the bimetallic sulfide solid solution could promote the intercalation of Al^{3+} into $Ni_{0.6}Co_{0.4}S$ composite cathode and further boost its aluminum storage capability.

Additionally, the mechanism of fast Al^{3+} diffusion in $Ni_{0.6}Co_{0.4}S$ was

also investigated by DFT calculations. Based on the above mentioned model with aluminum intercalated, the diffusion of Al^{3+} to the nearest vacancy site was simulated. As presented in Fig. 6a and b, the calculated diffusion barrier of Al^{3+} in $Ni_{0.6}Co_{0.4}S$ is 1.30 eV. While in CoS, the diffusion of Al^{3+} is hindered by 1.82 eV (Fig. 6c and d). In this way, diffusion dynamics could be enhanced in $Ni_{0.6}Co_{0.4}S$. These results prove that incorporation Ni^{2+} into CoS can effectively accelerate Al^{3+} migration, which presents the internal mechanism of $Ni_{0.6}Co_{0.4}S@MXene@NC$ cathode with improved performance.

In addition to the structural factors, another reason for the enhanced performance of $Ni_{0.6}Co_{0.4}S@MXene@NC$ cathode is the MXene and N-doped carbon dual protection layer. As shown in the SEM images, without MXene or N-doped carbon layer protection, $Ni_{0.6}Co_{0.4}S@NC$ underwent structure broken (Figs. S11a and b) and $Ni_{0.6}Co_{0.4}S@MXene$ suffered from active nanoparticles aggregation (Figs. S11c and d) after 100 cycles, respectively. While in the $Ni_{0.6}Co_{0.4}S@MXene@NC$ electrode, the structure still remained upon cycling (Fig. 6e). The TEM images further reflect the structural and composition stability of $Ni_{0.6}Co_{0.4}S@MXene@NC$. After 100 cycles, the morphology and structure of $Ni_{0.6}Co_{0.4}S@MXene@NC$ are well-maintained (Fig. 6f and g). Additionally, the corresponding element mappings of the cycled $Ni_{0.6}Co_{0.4}S@MXene@NC$ electrode (Fig. 6h) show that each element is homogeneously distributed, further demonstrating the high reaction reversibility and excellent structural stability. Moreover, the chemical stability of $Ni_{0.6}Co_{0.4}S@MXene@NC$ was investigated via immersing the separator containing the electrolyte disassembled from a fully discharged cell in anhydrous ethanol [23]. Interestingly, a light green color was observed for the compared $Ni_{0.6}Co_{0.4}S@NC$ (Fig. S12III), while
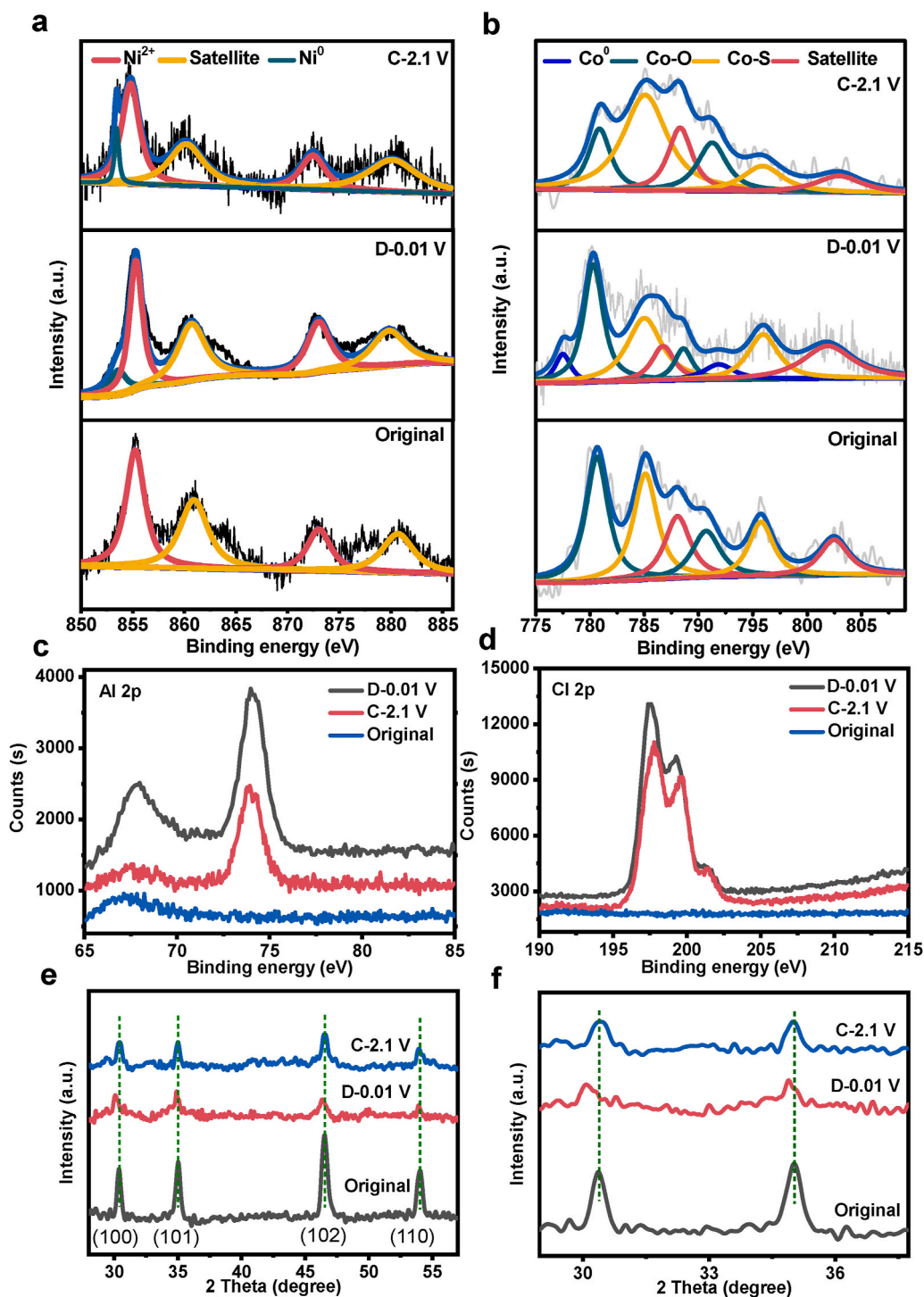
Fig. 5. Ex situ XPS data of the (a) Ni 2p, (b) Co 2p, (c) Al 2p, and (d) Cl 2p peaks for original, fully discharged and fully charged $Ni_{0.6}Co_{0.4}S@NC$. (e,f) Ex-situ XRD patterns of the $Ni_{0.6}Co_{0.4}S@NC$ at original, fully discharged and fully charged states.

almost no color change was observed for $Ni_{0.6}Co_{0.4}S@MXene@NC$ and a fresh electrolyte (Fig. S12II,I), respectively, indicating that the presence of MXene can effectively inhibit the shuttling and dissolution of active Co species [23]. Therefore, the high stability of the $Ni_{0.6}Co_{0.4}S@MXene@NC$ cathode can be ascribed to the inhibiting effect of MXene towards cobalt species dissolution and shuttling and the firm protective MXene@N-doped carbon armour which can buffer the volume expansion.

4. Conclusion

In summary, we have developed a unique bimetallic sulfide solid solution and dual protection strategy to fabricate MXene and N-doped carbon dual protected $Ni_{0.6}Co_{0.4}S$. Such well designed $Ni_{0.6}Co_{0.4}S@MXene@NC$ provides excellent platform for fine structural modulation towards significant enhancement of AIBs performance. The dissolution of Ni into CoS marrtix tunes its binding interaction with the Al^{3+} and modifies the Al^{3+} diffusion barrier. As a result, the $Ni_{0.6}Co_{0.4}S$ solid solution improves overall Al^{3+} storage capability, and contributes

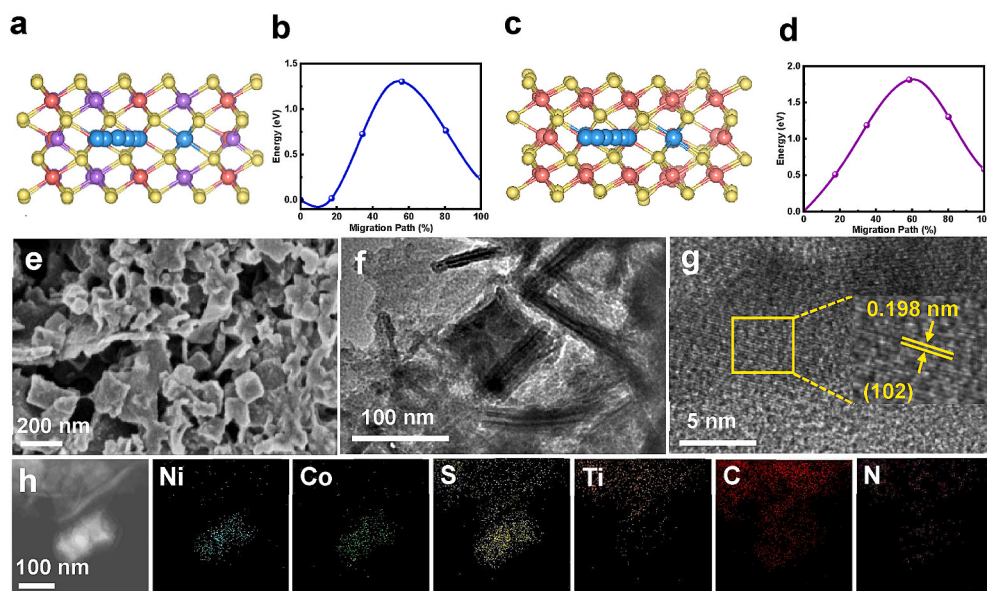**Fig. 6.** (a) Diffusion pathway of Al^{3+} in $Ni_{0.6}Co_{0.4}S$ and (b) corresponding energy profile. (c) Diffusion pathway of Al^{3+} in CoS and (d) corresponding energy profile. The red, purple, yellow and blue balls represent Co, Ni, S and Al atoms, respectively. (e) SEM, (f) TEM, (g) HRTEM images, and (h) elemental mapping images of $Ni_{0.6}Co_{0.4}S$@MXene@NC cathode after 100 cycles. (For interpretation of the references to color in this figure legend, the reader is referred to the Web version of this article.)

to fast Al^{3+} diffusion kinetics. Moreover, MXene and N-doped carbon dual protection structure can not only improve the structural stability and conductivity of the composite, but also prevent the dissolution of $Ni_{0.6}Co_{0.4}S$ towards the electrolyte. As a result, the designed AIBs cathode delivers enhanced electrochemical performance. Investigation into the aluminum storage mechanism of $Ni_{0.6}Co_{0.4}S$ cathode discloses its intercalation Al^{3+} into $Ni_{0.6}Co_{0.4}S$ to generate $Al_lNi_mCo_nS$ and elemental Ni and Co. This work promotes the process of enhancement of AIBs performance via smart designing and constructing cathode materials.

CRediT authorship contribution statement

Jiening Zheng: Conceptualization, Methodology, Investigation, Resources, Data curation, Formal analysis, Writing – original draft, Writing – review & editing. **Shunlong Ju:** Formal analysis. **Long Yao:** Conceptualization. **Guanglin Xia:** Conceptualization. **Xuebin Yu:** Validation, Methodology, Supervision, Project administration, Writing – review & editing, Funding acquisition.

Declaration of competing interest

The authors declare that they have no known competing financial interests or personal relationships that could have appeared to influence the work reported in this paper.

Acknowledgements

Appendix A. Supplementary data

Supplementary data to this article can be found online at https://doi.org/10.1016/j.jpowsour.2021.230450.

References

[1] C.P. Grey, J.M. Tarascon, Sustainability and in situ monitoring in battery development, Nat. Mater. 16 (1) (2017) 45–56, https://doi.org/10.1038/nmat4777.

[2] Y. Liu, Z. Tai, T. Zhou, V. Sencadas, J. Zhang, L. Zhang, K. Konstantinov, Z. Guo, H. K. Liu, An all-integrated anode via interlinked chemical bonding between double-shelled–yolk-structured silicon and binder for lithium-ion batteries, Adv. Mater. 29 (44) (2017), 1703028, https://doi.org/10.1002/adma. 201703028.

[3] Y. Wang, R. Chen, T. Chen, H. Lv, G. Zhu, L. Ma, C. Wang, Z. Jin, J. Liu, Emerging non-lithium ion batteries, Energy Storage Mater 4 (2016) 103–129, https://doi.org/10.1016/j.ensm.2016.04.001.

[4] F. Yang, H. Gao, J. Hao, S. Zhang, P. Li, Y. Liu, J. Chen, Z. Guo, Yolk–shell structured FeP@C nanoboxes as advanced anode materials for rechargeable lithium-/potassium-ion batteries, Adv. Funct. Mater. 29 (16) (2019), 1808291, https://doi.org/10.1002/adfm.201808291.

[5] G.A. Elia, K. Marquardt, K. Hoeppner, S. Fantini, R. Lin, E. Knipping, W. Peters, J.-F. Drillet, S. Passerini, R. Hahn, An overview and future perspectives of aluminum batteries, Adv. Mater. 28 (35) (2016) 7564–7579, https://doi.org/10.1002/adma.201601357.

[6] H. Yang, H. Li, J. Li, Z. Sun, K. He, H.-M. Cheng, F. Li, The rechargeable aluminum battery: opportunities and challenges, Angew. Chem. Int. Ed. 58 (35) (2019) 11978–11996, https://doi.org/10.1002/anie.201814031.

[7] M.-C. Lin, M. Gong, B. Lu, Y. Wu, D.-Y. Wang, M. Guan, M. Angell, C. Chen, J. Yang, B.-J. Hwang, H. Dai, An ultrafast rechargeable aluminium-ion battery, Nature 520 (7547) (2015) 324–328, https://doi.org/10.1038/nature14340.

[8] N.P. Stadie, S. Wang, K.V. Kravchyk, M.V. Kovalenko, Zeolite-templated carbon as an ordered microporous electrode for aluminum batteries, ACS Nano 11 (2) (2017) 1911–1919, https://doi.org/10.1021/acsnano.6b07995.

[9] Y. Hu, D. Ye, B. Luo, H. Hu, X. Zhu, S. Wang, L. Li, S. Peng, L. Wang, A binder-free and free-standing cobalt sulfide@carbon nanotube cathode material for aluminum-ion batteries, Adv. Mater. 30 (2) (2018), 1703824, https://doi.org/10.1002/adma.201703824.

[10] F. Wu, H. Yang, Y. Bai, C. Wu, Paving the path toward reliable cathode materials for aluminum-ion batteries, Adv. Mater. 31 (16) (2019), 1806510, https://doi.org/10.1002/adma.201806510.

[11] H. Li, H. Yang, Z. Sun, Y. Shi, H.-M. Cheng, F. Li, A highly reversible Co_3S_4 microsphere cathode material for aluminum-ion batteries, Nano Energy 56 (2019) 100–108, https://doi.org/10.1016/j.nanoen.2018.11.045.

[12] J. Jiang, H. Li, T. Fu, B.-J. Hwang, X. Li, J. Zhao, One-dimensional $Cu_{2-x}Se$ nanorods as the cathode material for high-performance aluminum-ion battery, ACS Appl. Mater. Interfaces 10 (21) (2018) 17942–17949, https://doi.org/10.1021/acsami.8b03259.

[13] Y. Ai, S.-C. Wu, K. Wang, T.-Y. Yang, M. Liu, H.-J. Liao, J. Sun, J.-H. Chen, S.-Y. Tang, D.C. Wu, T.-Y. Su, Y.-C. Wang, H.-C. Chen, S. Zhang, W.-W. Liu, Y.-Z. Chen, L. Lee, J.-H. He, Z.M. Wang, Y.-L. Chueh, Three-dimensional molybdenum diselenide helical nanorod arrays for high-performance aluminum-ion batteries, ACS Nano 14 (7) (2020) 8539–8550, https://doi.org/10.1021/acsnano.0c02831.

[14] C.G. Hawkins, A. Verma, W. Horbinski, R. Weeks, P.P. Mukherjee, L. Whittaker-Brooks, Decreasing the ion diffusion pathways for the intercalation of multivalent cations into one-dimensional TiS_2 nanobelt arrays, ACS Appl. Mater. Interfaces 12 (19) (2020) 21788–21798, https://doi.org/10.1021/acsami.9b21702.

[15] Z. Yu, Z. Kang, Z. Hu, J. Lu, Z. Zhou, S. Jiao, Hexagonal NiS nanobelts as advanced cathode materials for rechargeable Al-ion batteries, Chem. Commun. 52 (68) (2016) 10427–10430, https://doi.org/10.1039/C6CC05974K.

[16] Z. Hu, K. Zhi, Q. Li, Z. Zhao, H. Liang, X. Liu, J. Huang, C. Zhang, H. Li, X. Guo, Two-dimensionally porous cobalt sulfide nanosheets as a high-performance cathode for aluminum-ion batteries, J. Power Sources 440 (2019), 227147, https://doi.org/10.1016/j.jpowsour.2019.227147.

[17] Y. Zheng, T. Zhou, X. Zhao, W.K. Pang, H. Gao, S. Li, Z. Zhou, H. Liu, Z. Guo, Atomic interface engineering and electric-field effect in ultrathin Bi₂MoO₆ nanosheets for superior lithium ion storage, Adv. Mater. 29 (26) (2017), 1700396, https://doi.org/10.1002/adma.201700396.

[18] G. Barik, S. Pal, Monolayer transition-metal dichalcogenide Mo₁₋ₓWₓS₂ Alloys as efficient anode materials for lithium-ion batteries, J. Phys. Chem. C 122 (45) (2018) 25837–25848, https://doi.org/10.1021/acs.jpcc.8b07876.

[19] J. Wang, L. Zhang, K. Sun, J. He, Y. Zheng, C. Xu, Y. Zhang, Y. Chen, M. Li, Improving ionic/electronic conductivity of MoS₂ Li-ion anode via manganese doping and structural optimization, Chem. Eng. J. 372 (2019) 665–672, https://doi.org/10.1016/j.cej.2019.04.203.

[20] L. Zhou, F. Xiong, S. Tan, Q. An, Z. Wang, W. Yang, Z. Tao, Y. Yao, J. Chen, L. Mai, Nickel-iron bimetallic diselenides with enhanced kinetics for high-capacity and long-life magnesium batteries, Nano Energy 54 (2018) 360–366, https://doi.org/10.1016/j.nanoen.2018.10.033.

[21] S. Huang, S. Fan, L. Xie, Q. Wu, D. Kong, Y. Wang, Y.V. Lim, M. Ding, Y. Shang, S. Chen, H.Y. Yang, Promoting highly reversible sodium storage of iron sulfide hollow polyhedrons via cobalt incorporation and graphene wrapping, Adv. Energy Mater. 9 (33) (2019), 1901584, https://doi.org/10.1002/aenm.201901584.

[22] X. Yue, G. Wang, A.M. Patil, X. An, Z. Xie, X. Hao, Z. Jiang, A. Abudula, G. Guan, A novel vanadium-mediated MoS₂ with metallic behavior for sodium ion batteries: achieving fast Na⁺ diffusion to enhance electrochemical kinetics, Chem. Eng. J. (2020), 128107, https://doi.org/10.1016/j.cej.2020.128107.

[23] T. Cai, L. Zhao, H. Hu, T. Li, X. Li, S. Guo, Y. Li, Q. Xue, W. Xing, Z. Yan, L. Wang, Stable CoSe₂/carbon nanodice@reduced graphene oxide composites for high-performance rechargeable aluminum-ion batteries, Energy Environ. Sci. 11 (9) (2018) 2341–2347, https://doi.org/10.1039/C8EE00822A.

[24] M. Naguib, M. Kurtoglu, V. Presser, J. Lu, J. Niu, M. Heon, L. Hultman, Y. Gogotsi, M.W. Barsoum, Two-dimensional nanocrystals produced by exfoliation of Ti₃AlC₂, Adv. Mater. 23 (37) (2011) 4248–4253, https://doi.org/10.1002/adma.201102306.

[25] J. Pang, R.G. Mendes, A. Bachmatiuk, L. Zhao, H.Q. Ta, T. Gemming, H. Liu, Z. Liu, M.H. Rummeli, Applications of 2D MXenes in energy conversion and storage systems, Chem. Soc. Rev. 48 (1) (2019) 72–133, https://doi.org/10.1039/C8CS00324F.

[26] L.-P. Lv, C.-F. Guo, W. Sun, Y. Wang, Strong surface-bound sulfur in carbon nanotube bridged hierarchical Mo₂C-based MXene nanosheets for lithium–sulfur batteries, Small 15 (3) (2019), 1804338, https://doi.org/10.1002/smll.201804338.

[27] K. Liang, R.A. Matsumoto, W. Zhao, N.C. Osti, I. Popov, B.P. Thapaliya, S. Fleischmann, K. Prenger, M. Tyagi, E. Mamontov, V. Augustyn, R.R. Unocic, A.P. Sokolov, S. Dai, P.T. Cummings, M. Naguib, Engineering the interlayer spacing by pre-intercalation for high performance supercapacitor MXene electrodes in room temperature ionic liquid, Adv. Funct. Mater. 2104007. https://doi.org/https://doi.org/10.1002/adfm.202104007.

[28] Z. Li, X. Wang, W. Zhang, S. Yang, Two-dimensional Ti₃C₂@CTAB-Se (MXene) composite cathode material for high-performance rechargeable aluminum batteries, Chem. Eng. J. 398 (2020), 125679, https://doi.org/10.1016/j.cej.2020.125679.

[29] X. Liang, Y. Rangom, C.Y. Kwok, Q. Pang, L.F. Nazar, Interwoven MXene nanosheet/carbon-nanotube composites as Li–S cathode hosts, Adv. Mater. 29 (3) (2017), 1603040, https://doi.org/10.1002/adma.201603040.

[30] X. Liang, A. Garsuch, L.F. Nazar, Sulfur cathodes based on conductive MXene nanosheets for high-performance lithium–sulfur batteries, Angew. Chem. Int. Ed. 54 (13) (2015) 3907–3911, https://doi.org/10.1002/anie.201410174.

[31] P.E. Blöchl, Projector augmented-wave method, Phys. Rev. B 50 (24) (1994) 17953–17979, https://doi.org/10.1103/PhysRevB.50.17953.

[32] G. Kresse, J. Hafner, Ab initio molecular dynamics for liquid metals, Phys. Rev. B 47 (1) (1993) 558–561, https://doi.org/10.1103/PhysRevB.47.558.

[33] J.P. Perdew, K. Burke, M. Ernzerhof, Generalized gradient approximation made simple, Phys. Rev. Lett. 77 (18) (1996) 3865–3868, https://doi.org/10.1103/PhysRevLett.77.3865.

[34] S.L. Dudarev, G.A. Botton, S.Y. Savrasov, C.J. Humphreys, A.P. Sutton, Electron-energy-loss spectra and the structural stability of nickel oxide: an LSDA+U study, Phys. Rev. B 57 (3) (1998) 1505–1509, https://doi.org/10.1103/PhysRevB.57.1505.

[35] A. Emly, A. Van der Ven, Mg Intercalation in layered and spinel host crystal structures for Mg batteries, Inorg. Chem. 54 (9) (2015) 4394–4402, https://doi.org/10.1021/acs.inorgchem.5b00188.

[36] A. Van der Ven, J.C. Thomas, Q. Xu, B. Swoboda, D. Morgan, Nondilute diffusion from first principles: Li diffusion in LiₓTiS₂, Phys. Rev. B 78 (10) (2008), 104306, https://doi.org/10.1103/PhysRevB.78.104306.

[37] T. Mueller, G. Hautier, A. Jain, G. Ceder, Evaluation of tavorite-structured cathode materials for lithium-ion batteries using high-throughput computing, Chem. Mater. 23 (17) (2011) 3854–3862, https://doi.org/10.1021/cm200753g.

[38] S. Ju, X. Chen, Z. Yang, G. Xia, X. Yu, Atomic scale understanding of aluminum intercalation into layered TiS₂ and its electrochemical properties, J. Energy Chem. 43 (2020) 116–120, https://doi.org/10.1016/j.jechem.2019.09.003.

[39] G. Henkelman, B.P. Uberuaga, H. Jónsson, A climbing image nudged elastic band method for finding saddle points and minimum energy paths, J. Chem. Phys. 113 (22) (2000) 9901–9904, https://doi.org/10.1063/1.1329672.

[40] T. Ruan, B. Wang, Y. Yang, X. Zhang, R. Song, Y. Ning, Z. Wang, H. Yu, Y. Zhou, D. Wang, H. Liu, S. Dou, Interfacial and electronic modulation via localized sulfurization for boosting lithium storage kinetics, Adv. Mater. 32 (17) (2020), 2000151, https://doi.org/10.1002/adma.202000151.

[41] B.-H. Hou, Y.-Y. Wang, D.-S. Liu, Z.-Y. Gu, X. Feng, H. Fan, T. Zhang, C. Lü, X.-L. Wu, N-doped carbon-coated Ni₁.₈Co₁.₂Se₄ nanoaggregates encapsulated in N-doped carbon nanoboxes as advanced anode with outstanding high-rate and low-temperature performance for sodium-ion half/full batteries, Adv. Funct. Mater. 28 (47) (2018), 1805444, https://doi.org/10.1002/adfm.201805444.

[42] P. Zhang, R.A. Soomro, Z. Guan, N. Sun, B. Xu, 3D carbon-coated MXene architectures with high and ultrafast lithium/sodium-ion storage, Energy Storage Mater 29 (2020) 163–171, https://doi.org/10.1016/j.ensm.2020.04.016.

[43] X. Wu, Z. Wang, M. Yu, L. Xiu, J. Qiu, Stabilizing the MXenes by carbon nanoplating for developing hierarchical nanohybrids with efficient lithium storage and hydrogen evolution capability, Adv. Mater. 29 (24) (2017), 1607017, https://doi.org/10.1002/adma.201607017.

[44] D. Zhao, R. Zhao, S. Dong, X. Miao, Z. Zhang, C. Wang, L. Yin, Alkali-induced 3D crinkled porous Ti₃C₂ MXene architectures coupled with NiCoP bimetallic phosphide nanoparticles as anodes for high-performance sodium-ion batteries, Energy Environ. Sci. 12 (8) (2019) 2422–2432, https://doi.org/10.1039/C9EE00308H.

[45] Y.-T. Liu, P. Zhang, N. Sun, B. Anasori, Q.-Z. Zhu, H. Liu, Y. Gogotsi, B. Xu, Self-assembly of transition metal oxide nanostructures on MXene nanosheets for fast and stable lithium storage, Adv. Mater. 30 (23) (2018), 1707334, https://doi.org/10.1002/adma.201707334.

[46] L. Yang, W. Hong, Y. Zhang, Y. Tian, X. Gao, Y. Zhu, G. Zou, H. Hou, X. Ji, Hierarchical NiS₂ modified with bifunctional carbon for enhanced potassium-ion storage, Adv. Funct. Mater. 29 (50) (2019), 1903454, https://doi.org/10.1002/adfm.201903454.

[47] H. Li, P. Wu, Y. Xiao, M. Shao, Y. Shen, Y. Fan, H. Chen, R. Xie, W. Zhang, S. Li, J. Wu, Y. Fu, B. Zheng, W. Zhang, F. Huo, Metal–organic frameworks as metal ion precursors for the synthesis of nanocomposites for lithium-ion batteries, Angew. Chem. Int. Ed. 59 (12) (2020) 4763–4769, https://doi.org/10.1002/anie.201915279.

[48] H. Hong, J. Liu, H. Huang, C. Atangana Etogo, X. Yang, B. Guan, L. Zhang, Ordered macro–microporous metal–organic framework single crystals and their derivatives for rechargeable aluminum-ion batteries, J. Am. Chem. Soc. 141 (37) (2019) 14764–14771, https://doi.org/10.1021/jacs.9b06957.

[49] S. Ding, B. Zhou, C. Chen, Z. Huang, P. Li, S. Wang, G. Cao, M. Zhang, Sulfur-rich (NH₄)₂Mo₃S₁₃ as a highly reversible anode for sodium/potassium-ion batteries, ACS Nano 14 (8) (2020) 9626–9636, https://doi.org/10.1021/acsnano.0c00101.

[50] H. Ye, L. Wang, S. Deng, X. Zeng, K. Nie, P.N. Duchesne, B. Wang, S. Liu, J. Zhou, F. Zhao, N. Han, P. Zhang, J. Zhong, X. Sun, Y. Li, Y. Li, J. Lu, Amorphous MoS₃ infiltrated with carbon nanotubes as an advanced anode material of sodium-ion batteries with large gravimetric, areal, and volumetric capacities, Adv. Energy Mater. 7 (5) (2017), 1601602, https://doi.org/10.1002/aenm.201601602.

[51] D. Cao, W. Kang, S. Wang, Y. Wang, K. Sun, L. Yang, X. Zhou, D. Sun, Y. Cao, In situ N-doped carbon modified (Co₀.₅Ni₀.₅)₉S₈ solid-solution hollow spheres as high-capacity anodes for sodium-ion batteries, J. Mater. Chem. A 7 (14) (2019) 8268–8276, https://doi.org/10.1039/C9TA00709A.

[52] H. Huang, J. Cui, G. Liu, R. Bi, L. Zhang, Carbon-coated MoSe₂/MXene hybrid nanosheets for superior potassium storage, ACS Nano 13 (3) (2019) 3448–3456, https://doi.org/10.1021/acsnano.8b09548.

[53] Y. Song, Z. Sun, Z. Fan, W. Cai, Y. Shao, G. Sheng, M. Wang, L. Song, Z. Liu, Q. Zhang, J. Sun, Rational design of porous nitrogen-doped Ti₃C₂ MXene as a multifunctional electrocatalyst for Li–S chemistry, Nano Energy 70 (2020), 104555, https://doi.org/10.1016/j.nanoen.2020.104555.

[54] S. Wang, Z. Yu, J. Tu, J. Wang, D. Tian, Y. Liu, S. Jiao, A novel aluminum-ion battery: Al/AlCl₃-[EMIm]Cl/Ni₃S₂@Graphene, Adv. Energy Mater. 6 (13) (2016), 1600137, https://doi.org/10.1002/aenm.201600137.

[55] S. Wang, S. Jiao, J. Wang, H.-S. Chen, D. Tian, H. Lei, D.-N. Fang, High-performance aluminum-ion battery with CuS@C microsphere composite cathode, ACS Nano 11 (1) (2017) 469–477, https://doi.org/10.1021/acsnano.6b06446.

[56] Y. Hu, B. Luo, D. Ye, X. Zhu, M. Lyu, L. Wang, An innovative freeze-dried reduced graphene oxide supported SnS₂ cathode active material for aluminum-ion batteries, Adv. Mater. 29 (48) (2017), 1606132, https://doi.org/10.1002/adma.201606132.

[57] X. Xiao, M. Wang, J. Tu, Y. Luo, S. Jiao, Metal–organic framework-derived Co₃O₄@MWCNTs polyhedron as cathode material for a high-performance aluminum-ion battery, ACS Sustain. Chem. Eng. 7 (19) (2019) 16200–16208, https://doi.org/10.1021/acssuschemeng.9b03159.

[58] W. Liu, S. Ju, X. Yu, Phosphorus-amine-based synthesis of nanoscale red phosphorus for application to sodium-ion batteries, ACS Nano 14 (1) (2020) 974–984, https://doi.org/10.1021/acsnano.9b08282.

[59] W. Xing, W. Li, T. Cai, Y. Zhang, P. Bai, J. Xu, H. Hu, M. Wu, Q. Xue, Y. Zhao, J. Zhou, S. Zhuo, X. Gao, Z. Yan, Layered double hydroxides derived NiCo-sulfide as a cathode material for aluminum-ion batteries, Electrochim. Acta 344 (2020), 136174, https://doi.org/10.1016/j.electacta.2020.136174.

[60] W. Yang, H. Lu, Y. Cao, B. Xu, Y. Deng, W. Cai, Flexible free-standing MoS₂/carbon nanofibers composite cathode for rechargeable aluminum-ion batteries, ACS Sustain. Chem. Eng. 7 (5) (2019) 4861–4867, https://doi.org/10.1021/acssuschemeng.8b05292.